



The effects of a tilted FE-I4 3D sensor on clustering and charge deposition.

Simon De Ridder
Supervisor: Igor Rubinskiy

September 11, 2014

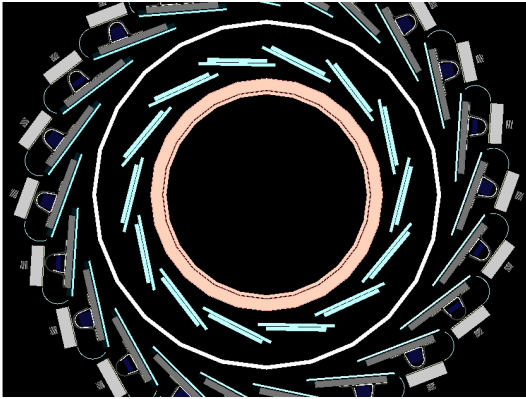
Abstract

An ATLAS FE-I4 pixel detector module with a 3D sensor, as used in the ATLAS IBL upgrade, was examined under various tilt angles using the EUDET pixel beam telescope at DESY. Despite the lower statistics at higher tilt angles, the behaviour of the sensor is seen to behave as one would expect. The length and deposited charge of a cluster of pixels is seen to increase at higher angles.

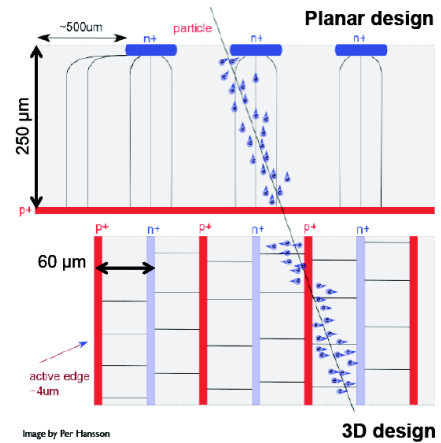
1 Introduction

1.1 The ATLAS IBL upgrade

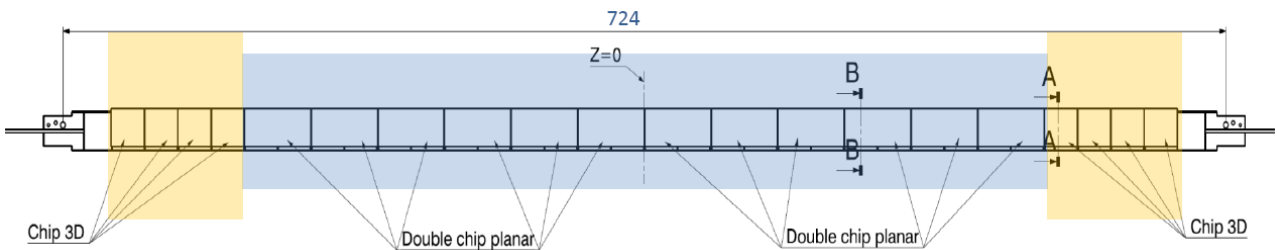
From February 2013 the Large Hadron Collider (LHC) at CERN has been shut down, and is planned to resume operation early 2015. Since that the ATLAS detector has been equipped with an upgrade to its pixel tracker. A fourth and more narrow pixel layer has been inserted around a smaller beam-pipe, and into the previous pixel detector. This new layer is called the Insertable B-Layer (IBL). It consists of 14 long tilted staves, each of which is 64 cm long (see figure 1d). They are tilted sideways by 14° , in order for them to overlap. These staves hold new pixel sensors whose center is at a distance of 33 mm from the beam-line.



(d) The new IBL around the new beam-pipe, surrounded by the previous beam-pipe for comparison.[1]



(e) Comparison between electrode geometries of planar and 3D sensors.[2]



(f) Structure of IBL staffe, with planar (blue) and 3D (yellow) sensors.[3]

Each of the inserted staves provides a pseudorapidity coverage of $|\eta| < 2.5$. In figure 1f the general structure of one of these staves is shown. Here we can see that the central region, at low pseudorapidity, is covered with planar sensors, while both ends are equipped with 3D sensors. The difference between these two types of sensors are shown in figure 1e: in planar sensors the bias and collection electrodes are located at the front and back of the sensor bulk, while in 3D sensors they are positioned in columns inside the bulk. The planar sensors are a cheaper and more established technology and can also reach higher yields, whereas the 3D sensors feature a shorter distance between the electrodes, which makes for a faster collection time, a lower depletion voltage and good radiation hardness.

All of the sensors in the IBL upgrade are read out by the newly developed FE-I4 module. This module is a radical improvement upon its predecessor, the FE-I3 module. The FE-I4 module

is more radiation hard, which is necessary at the high luminosities so close to the beam-pipe. It also stores data locally in each pixel until triggering, which overcomes the main efficiency limitations of the FE-I3 module, which reads out columns first and then stores the data. These advantages allow for efficient use up to luminosities of $3 \times 10^{34} \text{ cm}^2\text{s}^{-1}$ at the IBL distance from the beam[4].

1.2 The EUDET pixel beam telescope

The EUDET project, funded by the European Union, focuses on detector research and development towards the International Linear Collider (ILC). An important part of this research and development is carried out by test-beam telescope (figure 1). The EUDET project built six of these telescopes from a common design. The one used to take data is located at DESY and was named Datura. This telescope is a pixel tracker with six sensor planes, between which a Device Under Test (DUT) can be placed to be tested. This testing can be done by reconstructing tracks from test-beam particles and extrapolating them to the center where the DUT is located. The six telescope planes are made up of Mimosas26 CMOS pixel detectors, which have a pixel pitch of $18.4 \mu\text{m}$, with 576 rows and 1152 columns, and allow for a fast readout of about 10000 frames/s[5]. Each of the planes reaches a single point resolution better than $4 \mu\text{m}$, and for six planes this leads to an extrapolation uncertainty in the center of around $2 \mu\text{m}$.

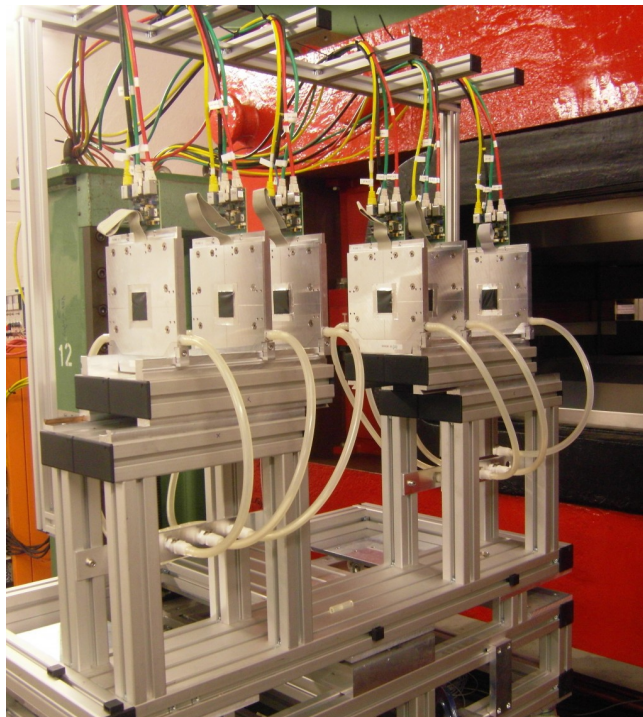


Figure 1: The EUDET pixel beam telescope at the DESY test-beam.[5]

In this project the EUDET telescope was used to analyse the behaviour of an FE-I4 module with a 3D sensor under various vertical tilt angles (figure 2), to assess the behaviour of these chips in the ATLAS IBL staves. This was done using an electron test-beam at DESY, with an energy of 4 GeV.

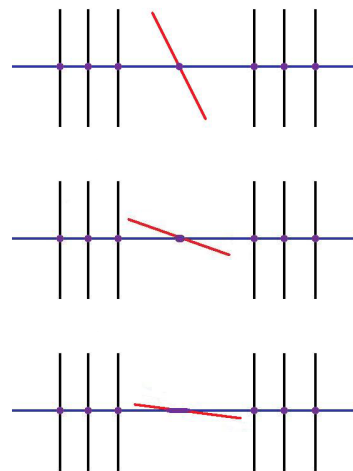


Figure 2: The telescope configuration and tilt direction.

2 The EU Telescope framework

As with any particle detector the raw sensor data needs to be reduced to physical variables belonging to the original particle entering the detector. For the telescope at DESY, this is done by the EU Telescope software, which is a collection of Marlin processors that can be called separately in a flexible and modular design. The Mimosa sensors have a built-in zero-suppression, so after a conversion of file format and masking of hot pixels, the fired pixels are the information to start with.

2.1 Clustering

Even though a particle might only traverse one sensor pixel, the electron-hole pairs it creates can migrate to the neighbouring pixels, and still produce a signal higher than the threshold. In order to take this effect into account, neighbouring fired clusters are combined into clusters.

2.2 Hitmaking

In a next step a guess of the position where the particle hit the sensor is made based on the size and shape of the cluster. The best guess is simply the center of the cluster. This never coincides exactly with the actual particle hit position, and the error between both can be varied by changing the threshold for pixels.

2.3 Alignment

The planes in the telescope are aligned up to millimeter scale, thanks to the supporting structure, but in general they are misaligned on the micrometer scale. In the Hitmaking step (2.2) a 'pre'-alignment can be done, by looking at correlations between the hits on consecutive planes. While this improves the alignment, the achieved accuracy is not quite good enough yet. This is why another alignment step can be taken. Apart from the newly developed GBL alignment (2.5), this can be achieved by fitting straight lines to the constructed hits, while letting the

alignment parameters (x-offset, y-offset and rotation around the beam direction) vary, and then minimising the χ^2 of all tracks at once, which then yields the best alignment parameters for this set of tracks.

2.4 Track reconstruction

Following alignment, the actual tracks are reconstructed. This can be done by fitting straight lines to the hits anew, but now with fixed, aligned sensors. Another approach is to use the so-called Deterministic Annealing Filter (DAF) method, which looks at groups of clusters and maximises the probability of them belonging to a track.

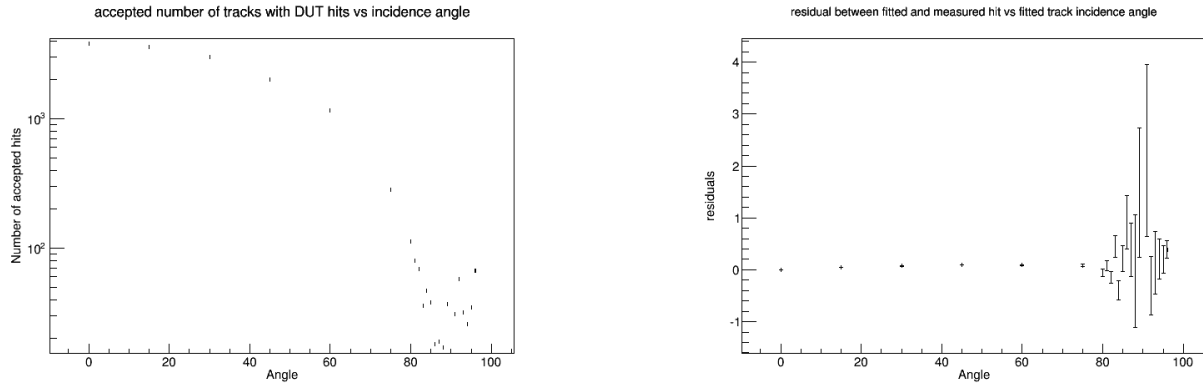
2.5 GBL

A new method for both alignment and track fitting has very recently been developed. It is called General Broken Lines (GBL) because it minimises the χ^2 of lines that are broken on so-called scattering planes, that model the scattering behaviour of both the air and the detector planes. It then solves the tracks as a set of vectors in the local frame of each plane, which can be propagated to the next by means of a propagation Jacobian. Alignment is then done in the same way as for straight line alignment, by varying the alignment parameters and minimising the χ^2 .

3 Results

3.1 Data analysis

In order to test the FE-I4 module with 3D sensors, it was placed in the EUDET pixel beam telescope (1.2) at high tilt angles. Unfortunately, in its current implementation, the straight line alignment does not take tilt angles into account. This is why it fails to provide the correct offsets for inclination angles larger than 45° . Since, at the time of writing, GBL is only just in a working stage, alignment was done by making various offsets for each tilt angle and choosing the offsets that produce the most fitted tracks in the track reconstruction stage. This is not an optimal solution, but it produces workable results. Because of the difficulties with even this method at high angles, the reconstructed number of tracks at incidence angles around 90° becomes quite small, and fluctuations on the residuals between measured hits and fitted track hits become quite large, as can be seen in figure 3.



(a) The number of reconstructed tracks with measured hits in function of track incidence angle.

(b) The average residual between measured hits and fitted track hits in local coordinates.

Figure 3: The effects of high tilt angles on the track reconstruction in the FE-I4

For these and the following plots the incidence angle of the tracks on the FE-I4 plane are those relative to the normal of the plane and in local coordinates. They were calculated using a fitted track hit on both the DUT (FE-I4) and the telescope plane before it (in direction of the beam), using the straight line between them. In appendix A the distributions of these incidence angles are given in both directions.

3.2 Cluster size

An interesting detector property to look at is the cluster size, meaning the length of a cluster in either pixel direction, in units of pixel length. In accordance with the ATLAS IBL, the FE-I4 was tilted along the direction of the long ($250\ \mu\text{m}$) side of the pixels. This means we can look at cluster size in this direction in function of the incidence angle in this direction, which has a small spread around the DUT incidence angle. In figure 4 we can see that a cluster size proportional to the tangent of the incidence angle can be expected.

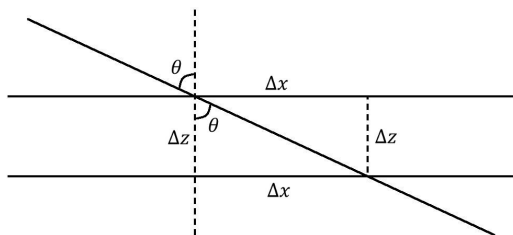


Figure 4: Schematic of the angular dependence of the cluster size.

On top of this a constant due to a finite spread of the deposited charge is to be expected, as is evident for perpendicular tracks. If a systematic error on the incidence angle is allowed, we arrive at the fit seen in figure 5.

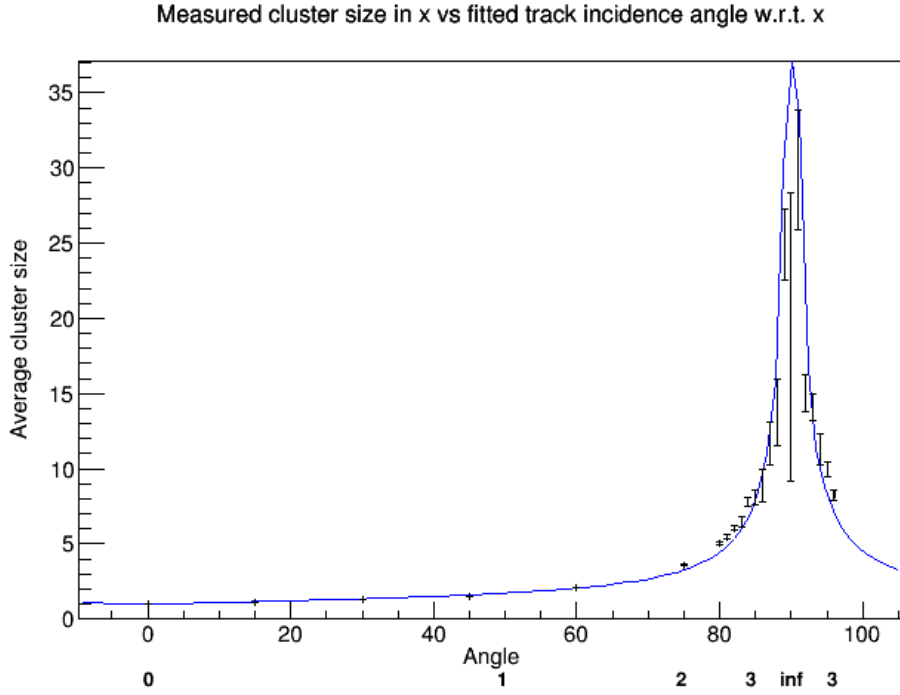


Figure 5: Cluster size in function of inclination angle

The fit yields (in units of pixel widths):

$$\Delta x = (0.997 \pm 0.003) + (0.616 \pm 0.005) \cdot \tan(\theta - (0.12 \pm 0.05)^\circ) \quad (1)$$

While the actual thickness of the sensor is 1 pixelwidth, this result hints that the effective thickness may be smaller, but the goodness of fit ($\chi^2/ndf = 35.8$) prevents from making such claims. The same analysis can be done along the short pixel direction, but as there is no tilt in this direction, the distribution is limited to small angles, and thus nearly flat (figure 6).

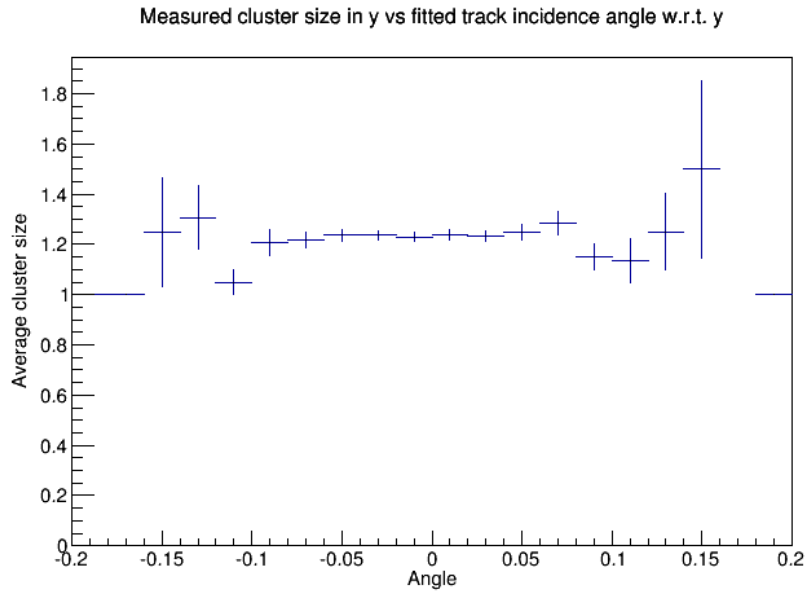


Figure 6: Cluster size in function of inclination angle in short pixel direction.

3.3 Time over Threshold

The FE-I4 module does not output a signal directly from the measured charge, but it measures how long a signal is larger than a certain threshold. This time is then converted into a 4 bit signal as an output (figure 7), which is then called the Time over Threshold (ToT). The reason why a 4 bit signal is used and not a 16 bit signal as in the FE-I3 module, is because of the higher required readout speed. This requires calibration in order to retrieve the deposited charge, but at larger deposited energies the relation becomes linear.

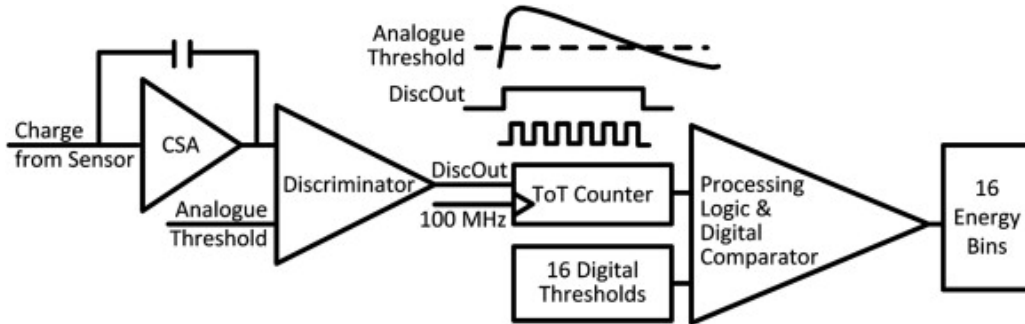


Figure 7: Schematic of the electronic conversion to ToT.

The ToT of the pixels in a cluster can be summed for each pixel row. In this way, an overview of the ToT along a cluster in the direction of a track can be displayed. Figure 8 shows the average of such displays for various incidence angles. As one would expect, the total deposited charge

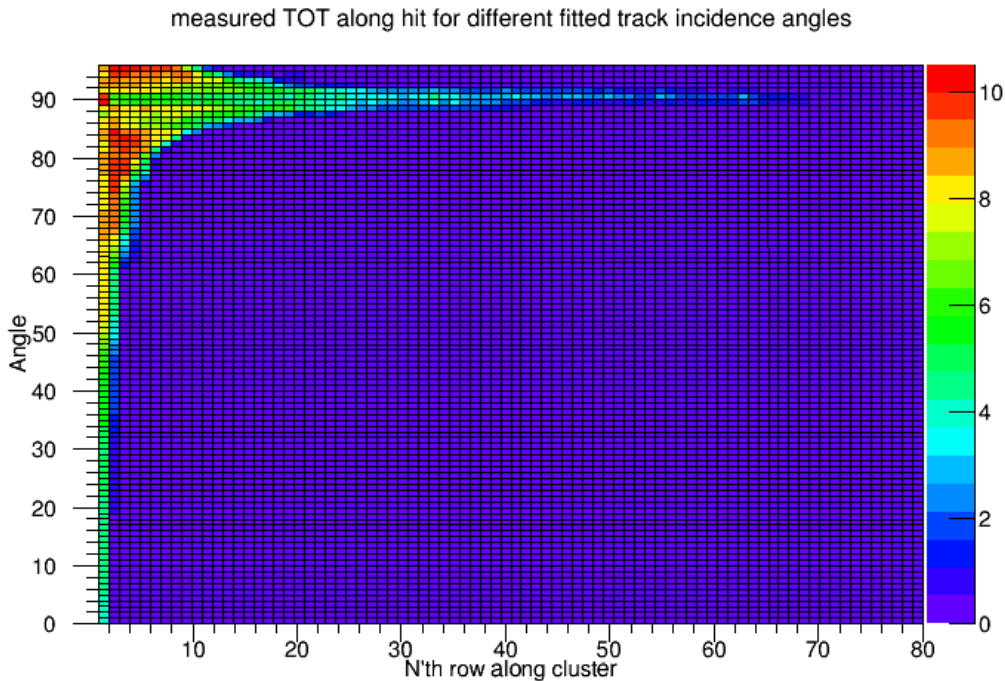


Figure 8: Measured ToT along a cluster in the track direction for various angles.

increases with the incidence angle. The position of maximal charge deposition also increases with the angle. At 90° the track would traverse the entire length of the sensor. However this

seems not to happen. One major reason may be the poor statistics at this angle. Another explanation is that the probability of an electron scattering out of the sensor plane becomes large, since the length of the sensor is about 21% of the radiation length in silicon (93.7 mm).

The same plot can be made in function of the more detector-oriented quantity pseudorapidity, which is defined as $\eta = -\ln(\tan(\theta/2))$, where θ is now not the incidence angle, but its complement. The result up to $\eta = 3.3$ can be seen in figure 9. Since the IBL staves are skewed by 14° to overlap, and the center of the sensors is 33,4 mm from the beam-line, the minimum and maximum radii of the sensors is $x_{min} = 32.4$ mm and $x_{max} = 36.8$ mm. With a longitudinal distance from the interaction point of positive and negative 249 mm up to 332 mm, the 3D sensor area spans the pseudorapidity range of $2.6 < \eta < 3.0$. In this range we see a significant amount of deposited charge along 6 to 11 pixel rows.

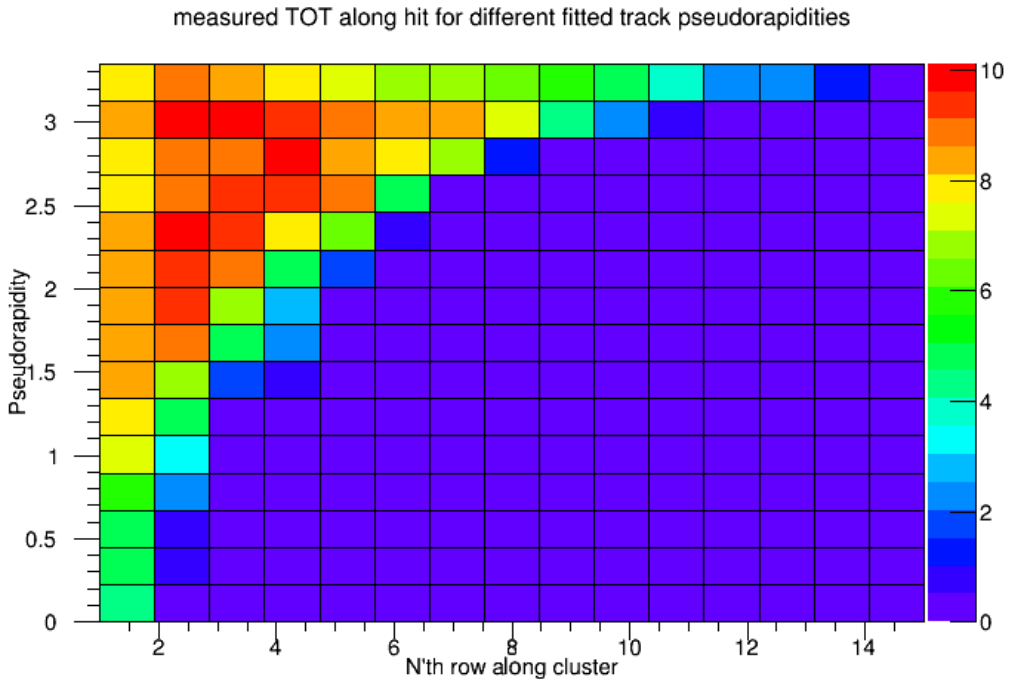


Figure 9: Measured ToT along a cluster in the track direction for various pseudorapidities.

3.4 Cluster charge

In a similar fashion as in 3.2, the total deposited charge in function of the incidence angle can be evaluated. This total cluster charge can be obtained by simply summing over the . If this charge is proportional to the length of the track in the sensor, a $1/\cos(\theta)$ -dependence would be expected. Figure 10 shows that this dependence seems to be valid ($\chi^2/ndf = 9.1$). The fit result in this case is (units of total ToT value):

$$Q = (7.8 \pm 0.1) + (7.43 \pm 0.08) \cdot \tan(\theta - (1.1 \pm 0.9) \cdot 10^{-5} \text{ }^\circ) \quad (2)$$

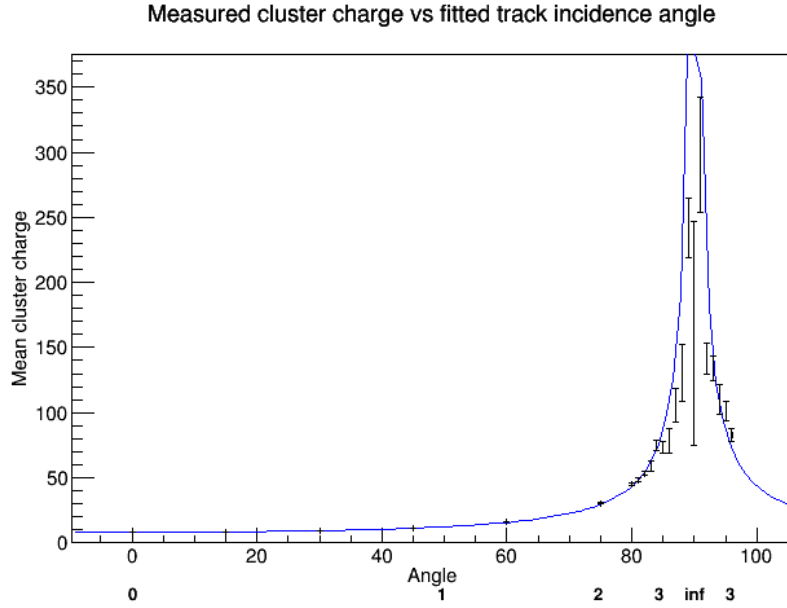


Figure 10: Total cluster charge in function of inclination angle.

The same trend can be seen in the distributions of the cluster charges for each run. These can be found in Appendix B. Up to about 82° there are enough statistics to compare these distributions. In figure 11 these distributions are plotted. The evolution towards larger cluster size is evident here.

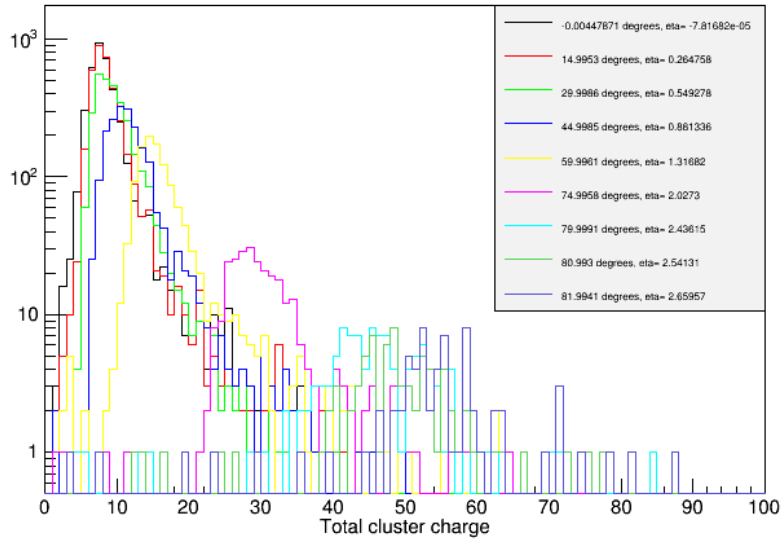


Figure 11: Total cluster charge distributions for incidence angles up to 82° .

Finally, the cluster charge can be plotted against the cluster size. From the mathematical approach used before a relationship of $\text{cluster charge} \propto \sqrt{(\text{cluster size})^2 + 1}$ would be expected, which strongly approaches a linear behaviour for large cluster sizes. This relationship can be found in figure 12, which means that the calibration of the ToT as a measure of deposited charge is indeed valid, at least up to the measured uncertainty.

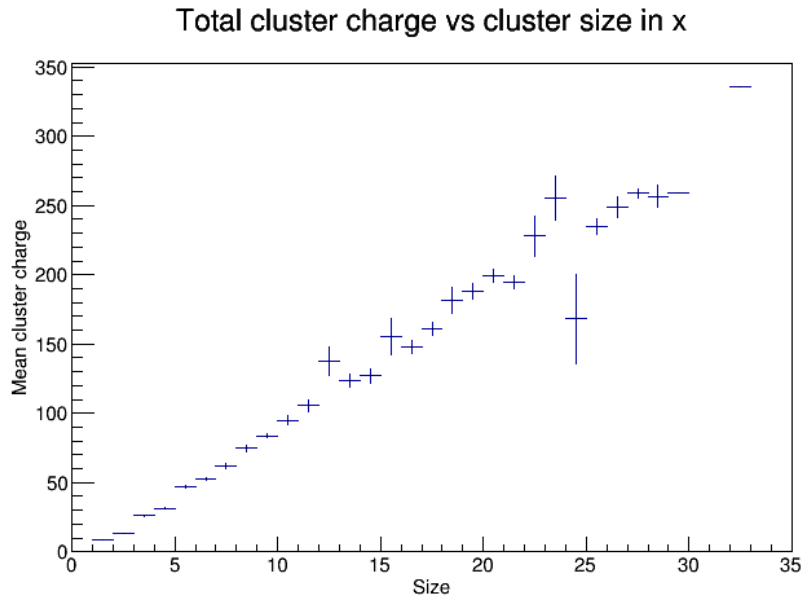


Figure 12: Total cluster charge against cluster size in the tilt direction.

4 Conclusion

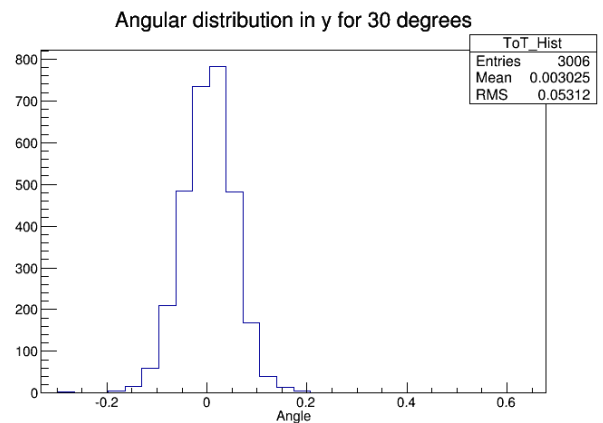
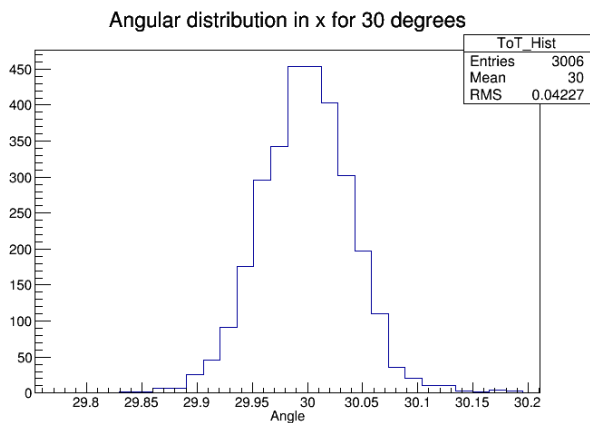
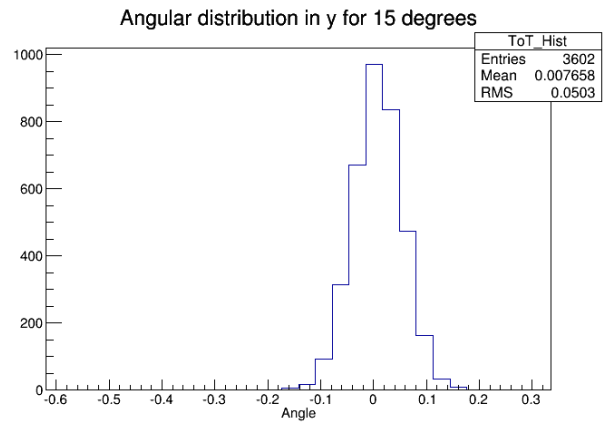
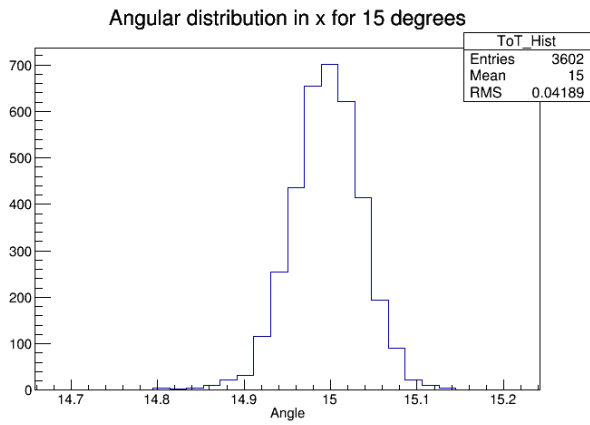
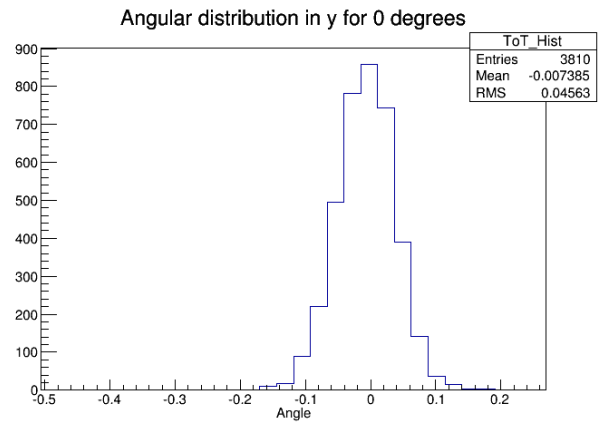
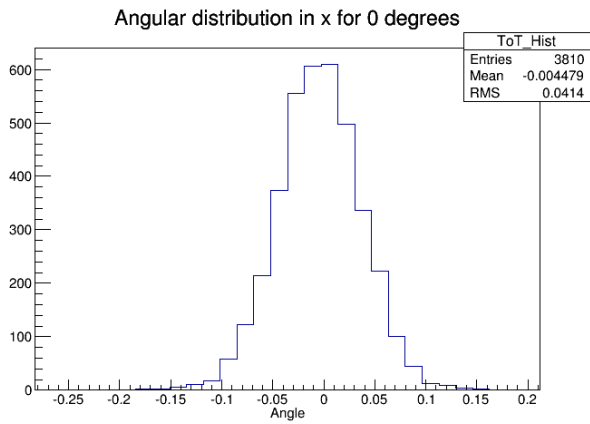
An analysis of data taken with a EUDET pixel beam telescope at DESY was performed for the newly installed ATLAS IBL FE-I4 module with 3D sensor under various tilt angles. Due to this tilt, problems arose concerning alignment, but they were resolved by performing the alignment manually. It was found that, as expected, the cluster size is roughly proportional to the tangent of the incidence angle. The total charge of a cluster also increases, proportional to the inverse of the cosine of the incidence angle. In order to further examine the behaviour of this module and sensor more statistics at higher angles are needed. In addition, a tilt along the short pixel direction could be introduced, to better compare with the conditions in the ATLAS IBL (tilted staves).

On a final note, I would like to thank Igor Rubinskiy, my supervisor, for his help guiding me through this project. My thanks also go to Alexander Morton, for general help and the development of GBL, almost in time, and to my fellow summer students Martin Klassen and Michael Nelson.

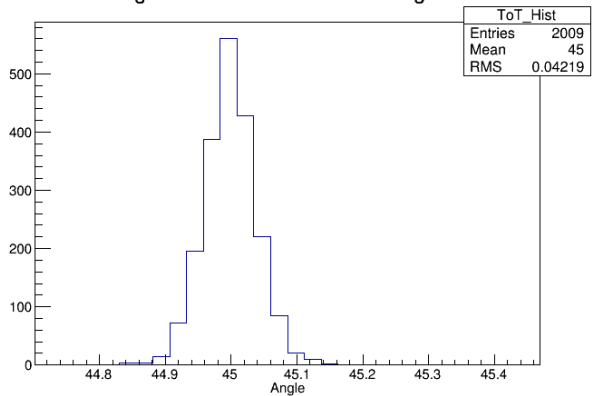
References

- [1] Gallrapp, Christian. "Overview of the ATLAS Insertable B-Layer (IBL) Project" *CERN*. CERN, 29 Feb. 2012. Web. 03 Sept. 2014 [<https://indico.cern.ch/event/161493/session/3/contribution/17/material/slides/0.pdf>].
- [2] Kocian, Martin. "ATLAS Pixel, phase 0 (IBL), Vertex 2012" *CERN*. SLAC, 26 Sept. 2012. Web. 03 Sept. 2014 [<http://indico.cern.ch/event/190941/session/9/contribution/38/material/slides/0.pdf>].
- [3] Ferrre, D. "IBL Project Overview" *CERN*. 9th Trento Workshop, Genova, 26-28 Feb. 2014. Web. 03 Sept. 2014 [<https://indico.cern.ch/event/273880/session/1/contribution/32/material/slides/1.pdf>].
- [4] The ATLAS IBL Collaboration. "Prototype ATLAS IBL Modules using the FE-I4A Front-End Readout Chip" arXiv:1209.1906 (2012): [physics.ins-det] Web. 03 Sept. 2014.
- [5] EUDET Consortium. "Infrastructure for Detector Research and Development towards the International Linear Collider" arXiv:1201.4657 (2012): [physics.ins-det] Web. 04 Sept. 2014.
- [6] Wong, W.S., et al. "A pixel detector asic for dosimetry using time-over-threshold energy measurements" *Radiation Measurements* 46 (2011): 1619-23 Web. 06 Sept. 2014.

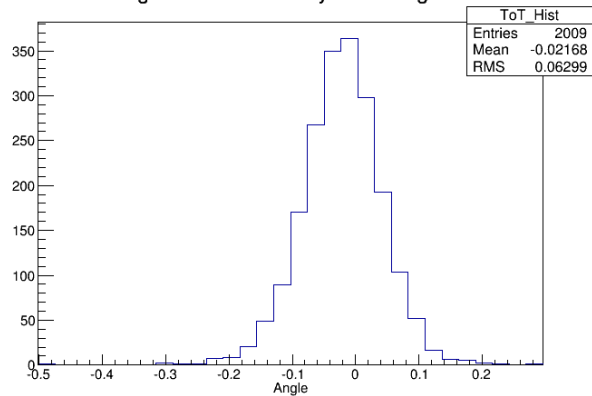
A Incidence Angle Distributions



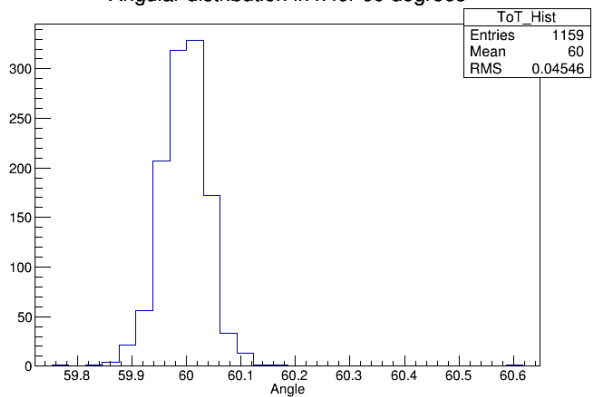
Angular distribution in x for 45 degrees



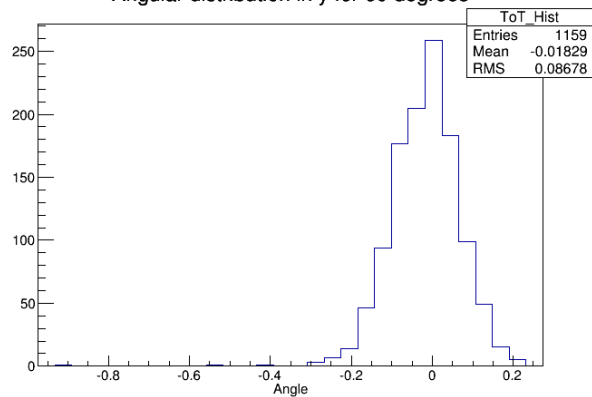
Angular distribution in y for 45 degrees



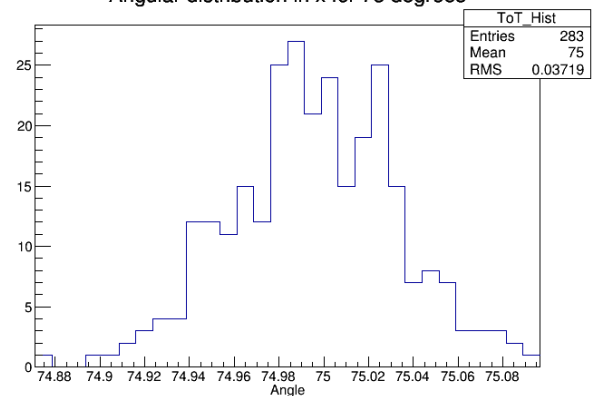
Angular distribution in x for 60 degrees



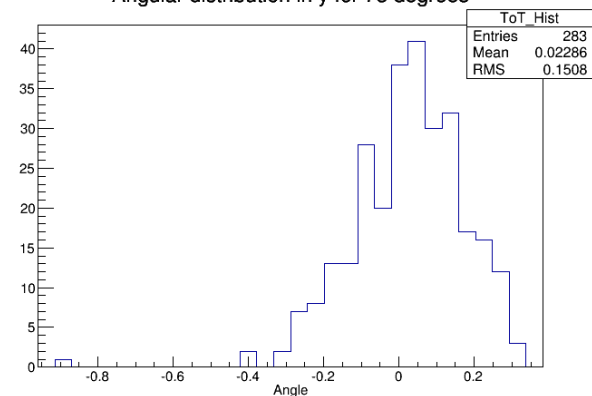
Angular distribution in y for 60 degrees



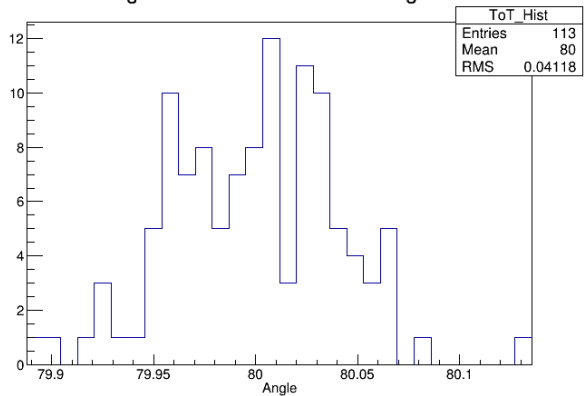
Angular distribution in x for 75 degrees



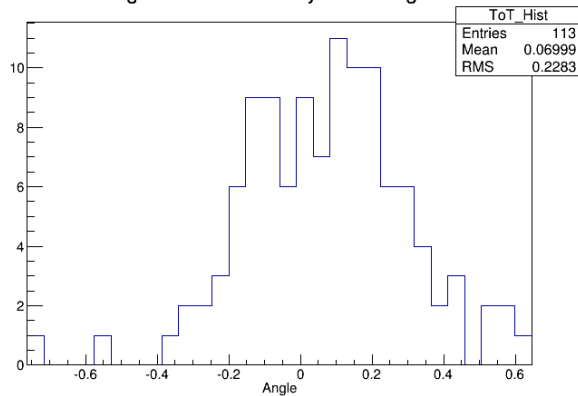
Angular distribution in y for 75 degrees



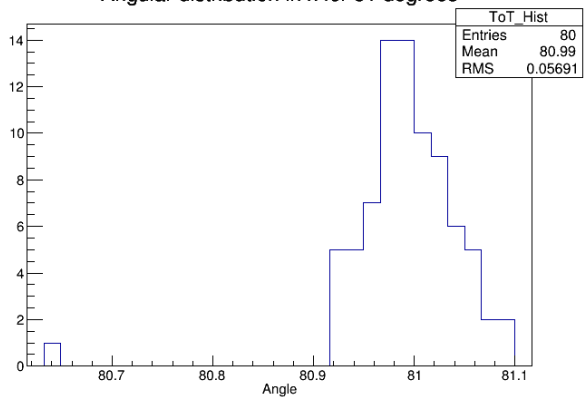
Angular distribution in x for 80 degrees



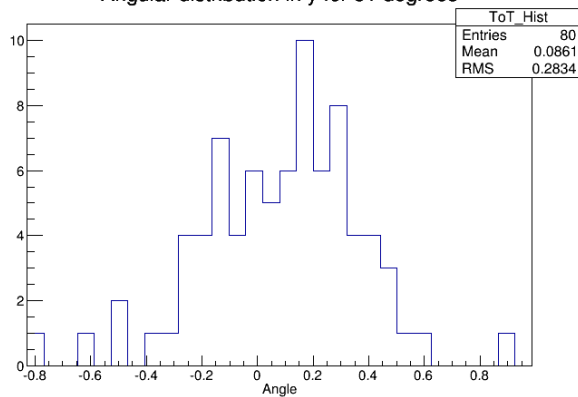
Angular distribution in y for 80 degrees



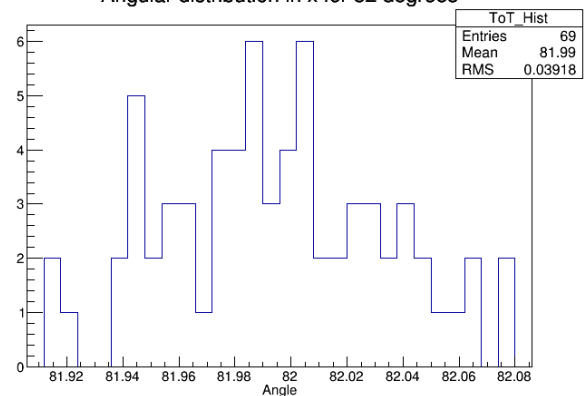
Angular distribution in x for 81 degrees



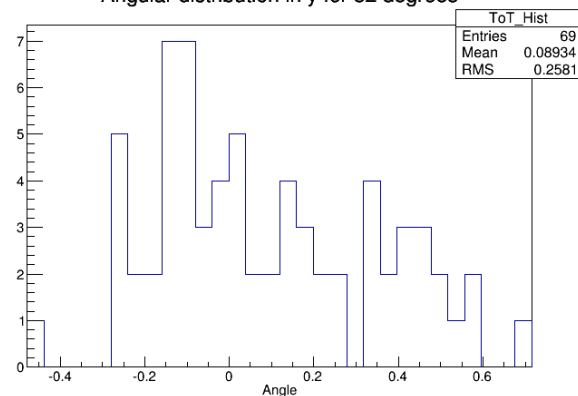
Angular distribution in y for 81 degrees



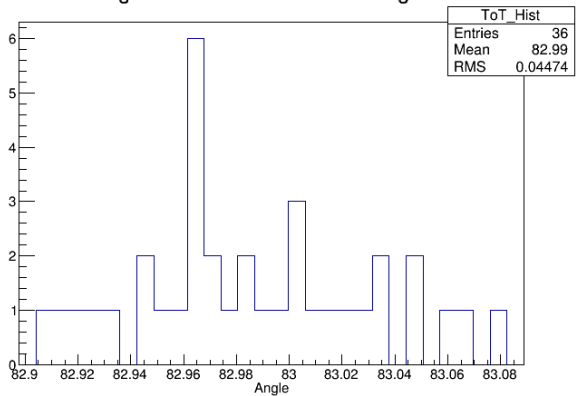
Angular distribution in x for 82 degrees



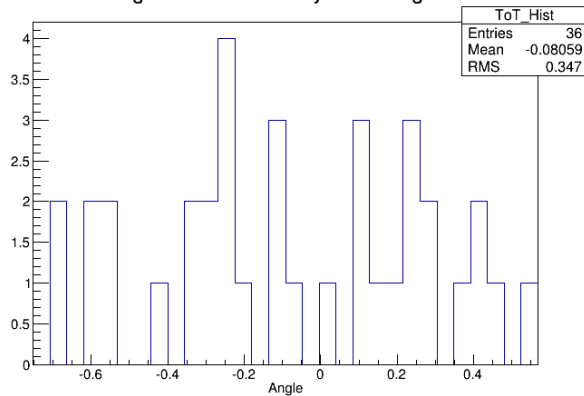
Angular distribution in y for 82 degrees



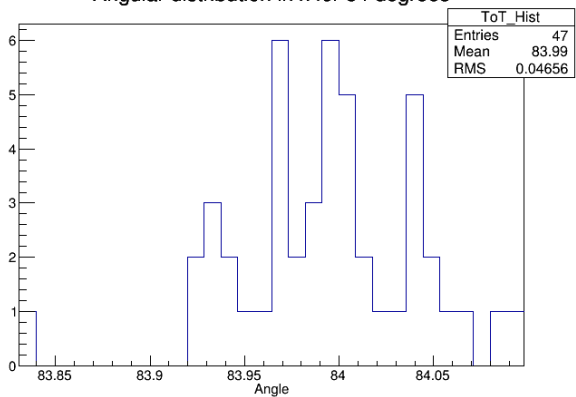
Angular distribution in x for 83 degrees



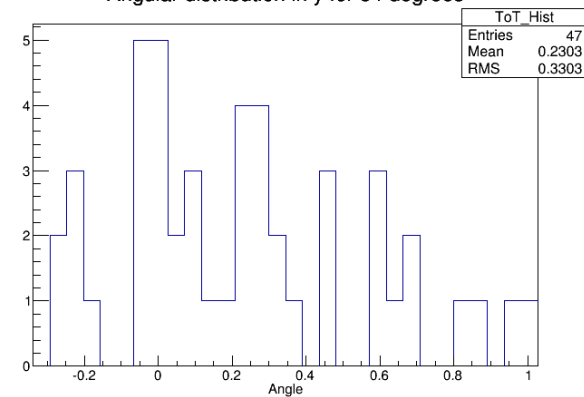
Angular distribution in y for 83 degrees



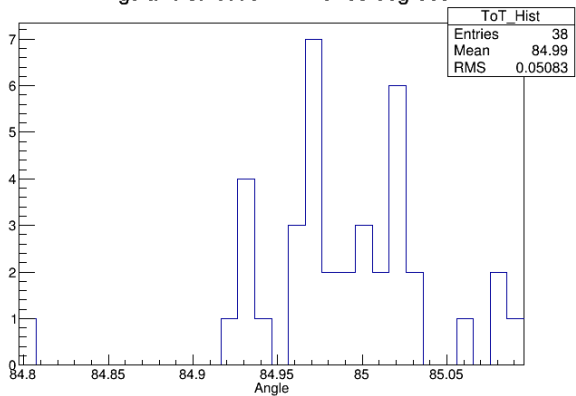
Angular distribution in x for 84 degrees



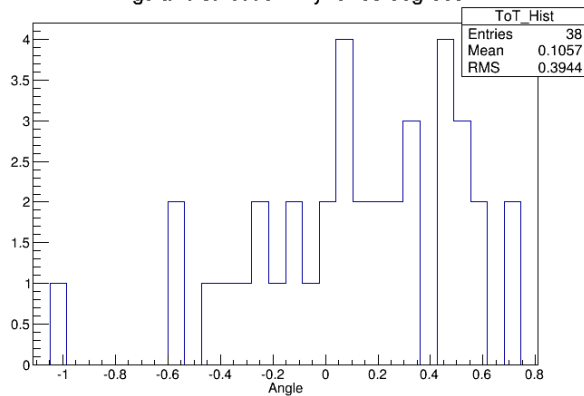
Angular distribution in y for 84 degrees



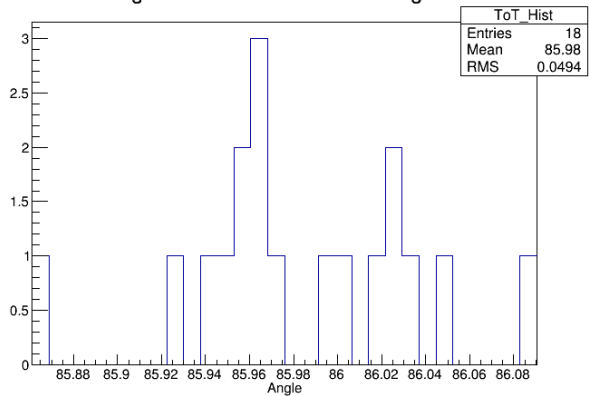
Angular distribution in x for 85 degrees



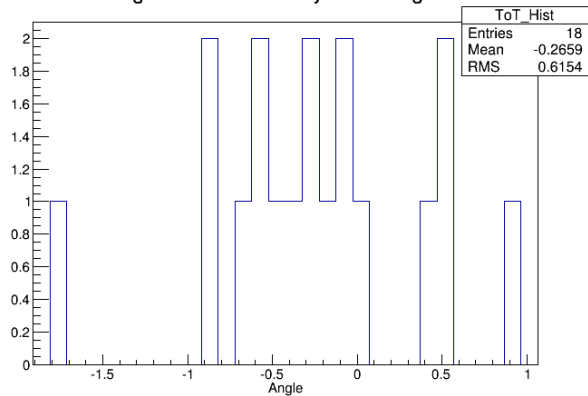
Angular distribution in y for 85 degrees



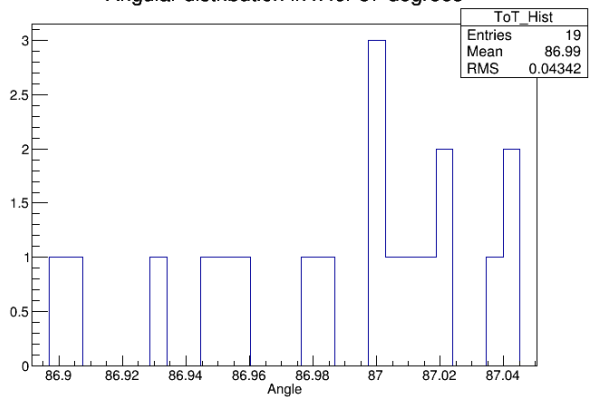
Angular distribution in x for 86 degrees



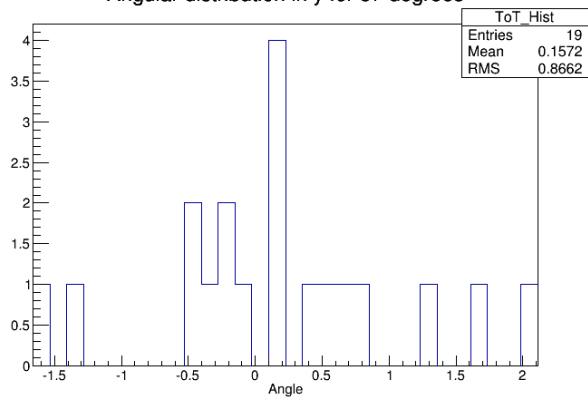
Angular distribution in y for 86 degrees



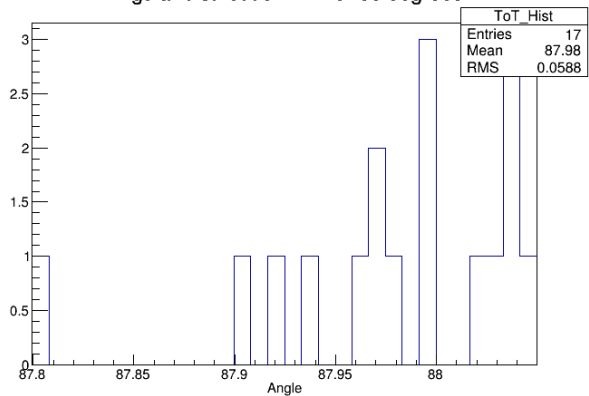
Angular distribution in x for 87 degrees



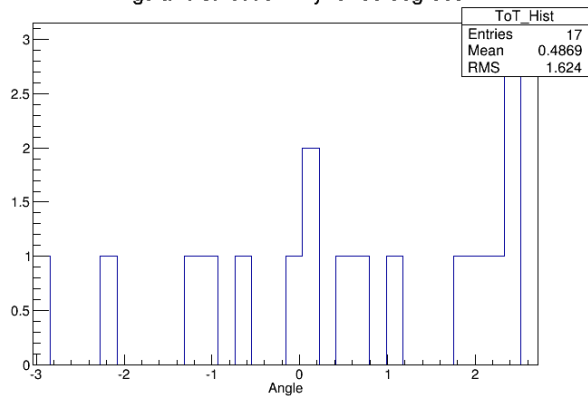
Angular distribution in y for 87 degrees



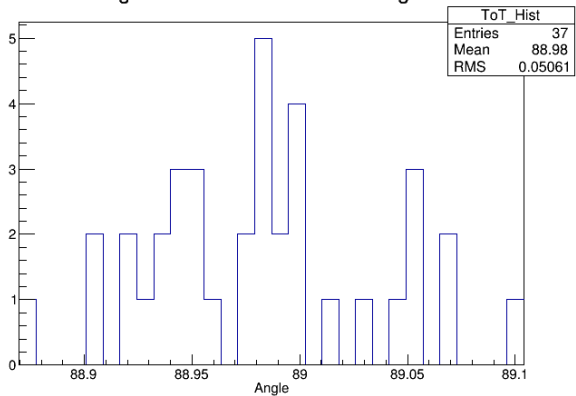
Angular distribution in x for 88 degrees



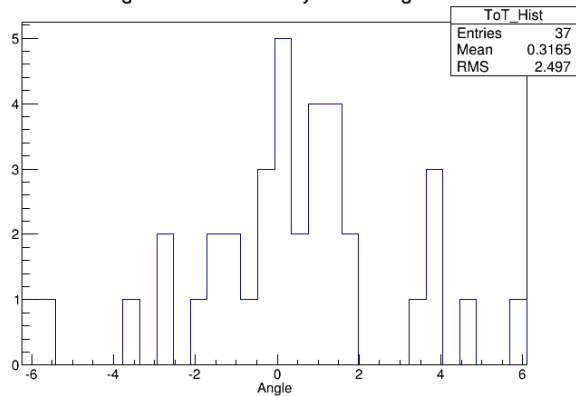
Angular distribution in y for 88 degrees



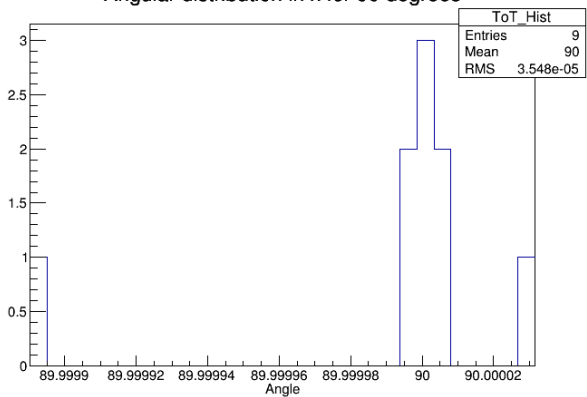
Angular distribution in x for 89 degrees



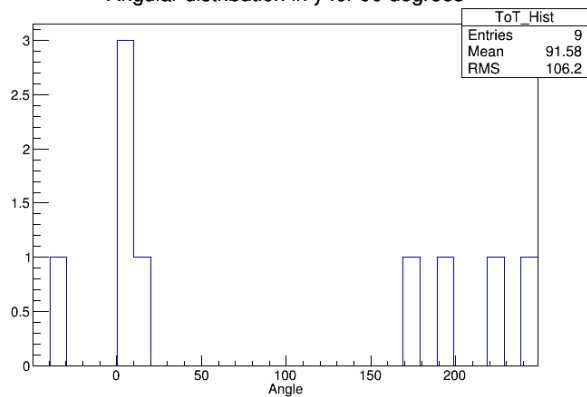
Angular distribution in y for 89 degrees



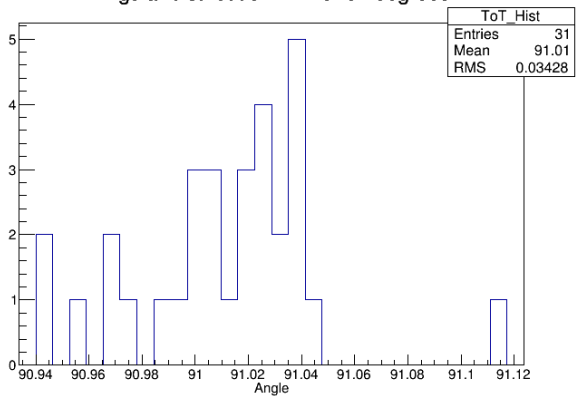
Angular distribution in x for 90 degrees



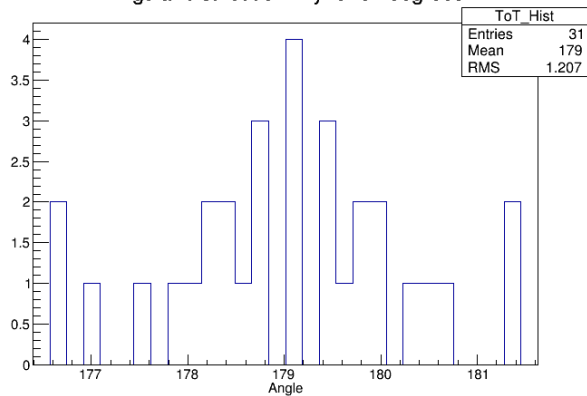
Angular distribution in y for 90 degrees



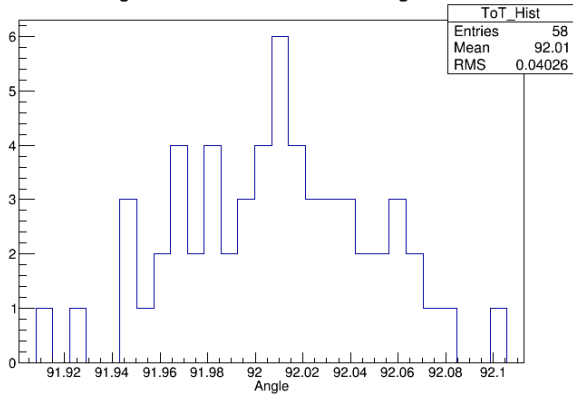
Angular distribution in x for 91 degrees



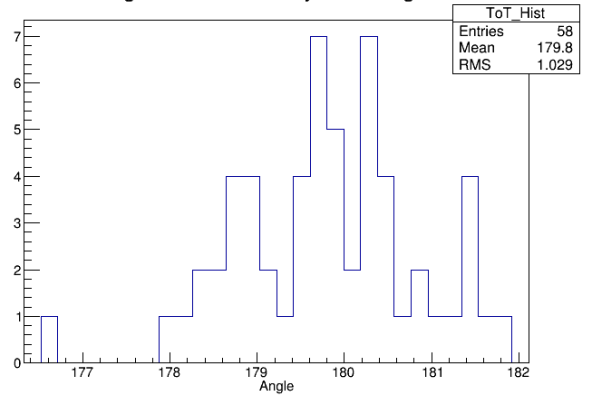
Angular distribution in y for 91 degrees



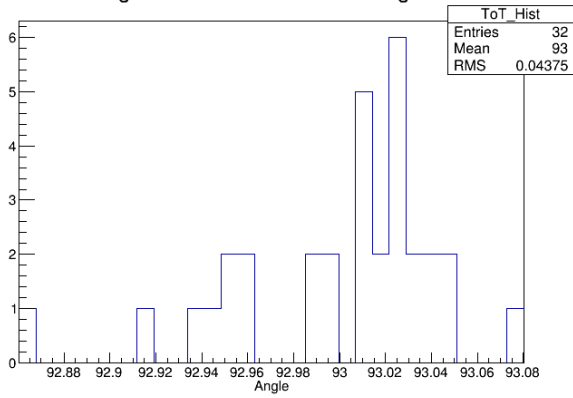
Angular distribution in x for 92 degrees



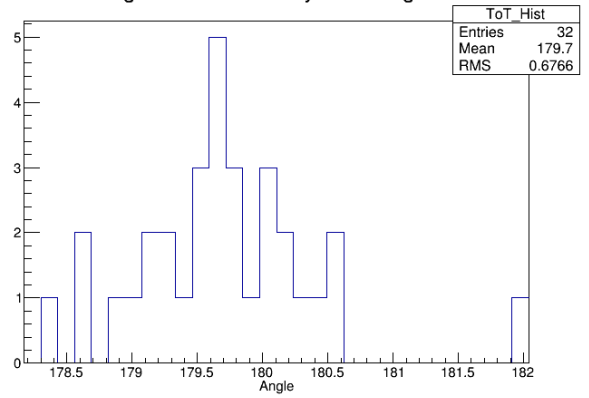
Angular distribution in y for 92 degrees



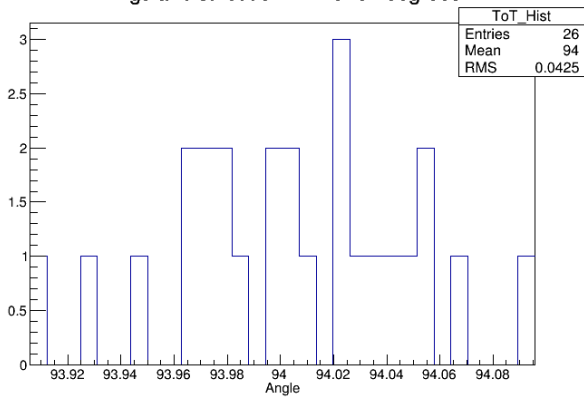
Angular distribution in x for 93 degrees



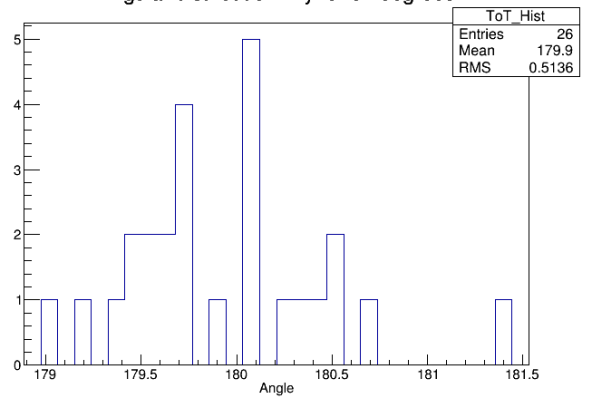
Angular distribution in y for 93 degrees



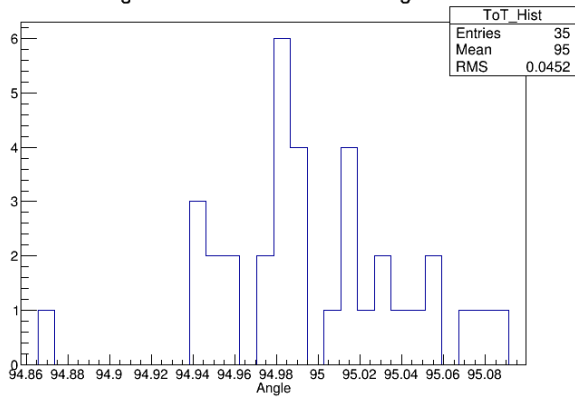
Angular distribution in x for 94 degrees



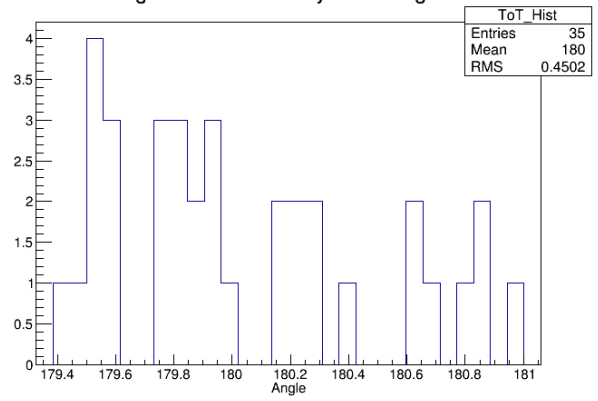
Angular distribution in y for 94 degrees



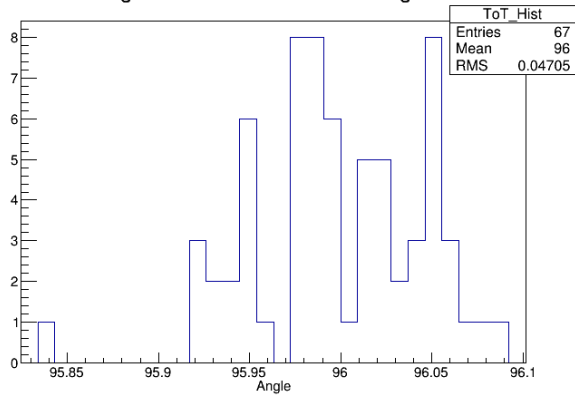
Angular distribution in x for 95 degrees



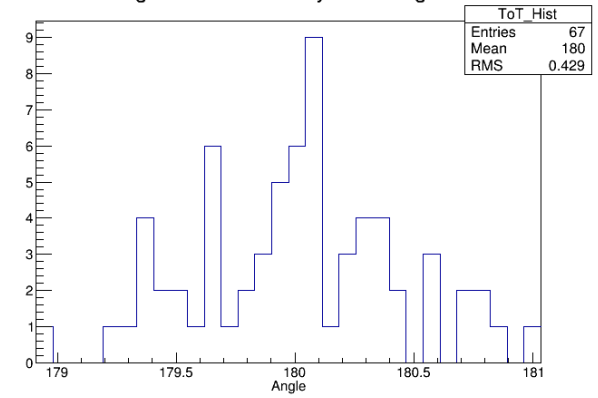
Angular distribution in y for 95 degrees



Angular distribution in x for 96 degrees



Angular distribution in y for 96 degrees



B Cluster Charge Distributions

